Visible-Infrared-Terahertz Optical Modulation of Few-Layer Graphene through Lithium Intercalation

Ganying Zeng(曾干英)[1,2], Zhenyu Fang(方振宇)[1,2], Weibao He (何韦宝)[3], Zixuan Wang(王孜炫)[1,2], Yijie Li(李怡洁)[1,2], Liantuan Xiao(肖连团)[1,2], Suotang Jia(贾锁堂)[1,2], Chengbing Qin(秦成兵)[1,2,*], and Renyan Zhang(张仁彦) [3,*]

[1] State Key Laboratory of Quantum Optics and Quantum Optics Devices, Institute of Laser Spectroscopy, Shanxi University, Taiyuan, Shanxi 030006, China.

[2] Collaborative Innovation Center of Extreme Optics, Shanxi University, Taiyuan, Shanxi 030006, China

[3] College of Advanced Interdisciplinary Studies, National University of Defense Technology, Changsha 410073, China;

*Corresponding author: chbqin@sxu.edu.cn; ryancms@sina.cn

Optical modulation is significant and ubiquitous to telecommunication technologies, smart windows, and military devices. However, due to the limited tunability of traditional doping, it is a tough problem to achieve broadband optical property change. Here, we demonstrate a remarkable transformation of optical transmittance in few-layer graphene (FLG) covering the electromagnetic spectrum from the visible to the terahertz wave after lithium (Li) intercalation. It results in that the transmittance is higher than 90% from the wavelength of 480 to 1040 nm and increases most from 86.4% to 94.1% at 600 nm, reduces from ~80% to ~68% in the wavelength range from 2.5 to 11 μm, and has ~20% reduction over a wavelength range from 0.4 THz to 1.2 THz and reduces from 97.2% to 68.2% at the wavelength of 1.2 THz. The optical modification of lithiated FLG is attributed to the increase of Fermi energy (E_f) due to the charge transfer from Li to graphene layers. Our results may provide a new strategy for the design of broadband optical modulation devices.

Keywords: few-layer graphene, intercalation, LiC_{12}, optical modulation, charge transfer

1. Introduction

Light modulation is an indispensable operation in the photics and photonics fields. Research on on-chip broadband optical modification is particularly appealing and yet challenging. Most traditional optical bulk crystals are applied to manipulate light, suffering from issues of bandwidth, loss, and integration[1]. Therefore, it has great significance for developing optical materials with compact, efficient, broadband response, and so on characteristics. Two-dimensional (2D) layered materials with atomic thickness, high carrier mobility, and large surface area, may create a unique combination to control on-chip light. Recently, many strategies, such as gate tuning[2, 3], defect design[4, 5], mechanical strain[6, 7], heterojunction construction[8], and anomalous refraction and planar focusing effect[9,10] have been proposed to engineer the band structure of 2D materials. Compared to these methods, intercalation reaction is generated in host interlayers, with charge transfer between host materials and guest species, making a more obvious Fermi level (E_f) shift than any others[11, 12]. Many excellent works have demonstrated that intercalation is a powerful tool to manipulate light-matter interaction[11, 13, 14]. For example, Zeng et al. found color changes and second-harmonic generation in multilayer graphene (about 150 layers) with Li or H_2SO_4 intercalation[15, 16], and nonlinear absorption effect transformation in few-layer graphene (about 6-8 layers) with Li intercalation[17]. Omer et al. produced a graphene optical surface and controlled the infrared emission via ionic liquid intercalation[18]. Wan et al. applied alkali-ion intercalation in a composite film of carbon nanotubes and reduced graphene, and transmittance had a ~20%-30% increase from visible (450 nm) to infrared (5 μm)[19].

Graphene has a unique linear energy and momentum dispersion relationship near the Diract point with zero gap, having intraband and interband transition two operation modes, which allows a broad-spectrum response range from ultraviolet, visible, and infrared to terahertz and microwave[20]. A. K. Geim et al. found that the optical absorption rate of single-layer graphene is 2.3% and calculated that the optical absorption of few-layer graphene (FLG) is proportional to the number of layers[21]. Therefore, an appropriate increase in the thickness of graphene can enhance the optical response. FLG presents a stacking of graphene layers with an interlayer spacing of 3.3 Å[22]. Owing to the strong covalent bonding (347 kJ/mol))[23] in the layers but with weak van der Waals interaction (16.7 kJ/mol)[24] between layers, FLG is considered an excellent host material that enables abundant ions to dwell in graphene interlayers. Metallic Li is a promising anode candidate for Li batteries. Due to the minimum radius in all of the metal elements[25] and electrons easily lost, Li-ions can rapidly shuttle between graphene layers. In addition, its high theoretical capacity of 3860 mAhg^{-1} can donate many electrons to host materials[26]. During the lithium-ion battery reaction process, large charge transfer occurs between the Li anode and graphene cathode, shifting E_f from 0 to 1.5[27] even 2 eV[28] for LiC_6. Therefore, Li intercalation should be able to operate optical properties in FLG

over a wide spectral bandwidth and with high modulation depth.

In this study, Li few-layer graphene intercalation compound (LiGIC) is prepared by galvanic reaction. Raman spectra, transmittance spectra, and optical images are used to investigate and understand the optical properties changes in FLG before and after Li intercalation. After Li intercalation, the formed LiGIC is proved to be LiC_{12}. We observe obvious optical transmittance changes in visible, infrared, and terahertz (THz) waves. The striking increase in sheet conductivity implies charge transfer between Li atoms and graphene layers, which will cause a move of the E_f of graphene. Hence, the behavior of the electron transition both in intraband and interband will be changed, leading to modifying properties in a broad range. Our result provides possibilities for optoelectronic applications based on 2D intercalated compounds in the broad-spectrum stealth regime.

2. Experiments

2.1 Preparation of few-layer graphene

The few-layer (6~8 layers) graphene was grown by chemical vapor deposition (CVD) on 50 μm thick copper (Cu) foils, which were purchased from SixCarbon Technology Shenzhen). The surface of FLG was spin-coated with 300 nm poly-methyl methacrylate (PMMA) film (2000rpm, 45s; PMMA A4, Microchem). Then, the PMMA/FLF/Cu was floated on the $FeCl_3$ saturated solution, and the Cu substrate was etched after about 6 hours. Afterward, the FLG film supported by PMMA was transferred to deionized water and cleaned thoroughly three times. A JGS1 quartz substrate was used to pick up the FLG/PMMA in the deionized water and the PMMA/FLG/JGS1 was dried in an oven at 80 °C for 6 hours. Next, it was immersed in acetone for 10 hours to remove the PMMA completely. After the FLG/JGS1 was fetched out of the acetone, it was immediately immersed in anhydrous ethanol for 30 s. Finally, we baked it in an oven at 80 °C to dry the remaining anhydrous ethanol and acetone.

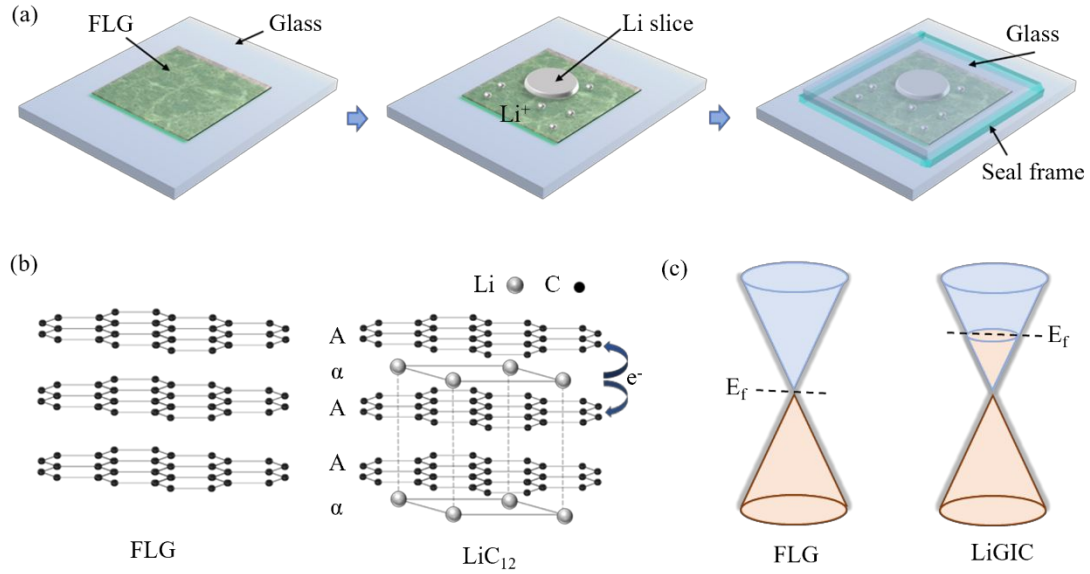### 2.2 Li intercalation and Device fabrication

The FLG on the JGS1 quartz substrate was transferred inside a glovebox (Super (1220/750/900), MIKROUNA, China) filled with an argon atmosphere. Then small Li metal was pressed on the surface of FLG and placed in a corner area of FLG. Then, A few drops of electrolyte ($LiPF_6$ in ethylene carbonate/diethyl carbonate, w/w = 1:1) were added and covered on the whole FLG. The lithiation reaction is based on the galvanic cell. Due to the cathode FLG and anode Li contact with each other, their interface acts as the lithiation reaction channel. The lithium reaction can be started with the electrolyte added and finished for several minutes. After that, the electrolyte is cleaned by the diethyl carbonate solvent. Next, a double-sided square frame tape is stuck to the substrate with the sample in the center of the frame, and another JGS1 quartz is placed on it.

2.3 Characterization and Measurement

The Raman spectra were acquired by a commercial MStarter 100 micro spectral scanning test system armed with an excitation laser of 532 nm. The collection and analysis of emitted signals is achieved by a spectrometer (ANDOR-rock). During measurement, we used a microscope objective with ×50 magnification to focus the laser on the surface of the FLG film through the top glass. The laser power was set to 2.8 mW. The sheet resistance of FLG and LiGIC was measured using a Keithley 2636B source meter (Tektronix, USA) and with the van der Pauw method. Visible optical absorption and transmittance spectra were performed by an angle-resolved spectrum system (Ideaoptics, China). Infrared absorption and transmittance spectra were recorded on a Fourier transform infrared spectrometer (FTIR, Thermo Scientific Nicolet IS50, USA). Large-scale thermal mapping could be measured with a FLIR T560 thermal camera, which allows broad wavelengths of 7.5-14 μm and has a high resolution of 640×480 pixels. Terahertz transmission was measured with an optical pump THz-probe (OPTP) setup. The mode-locked Ti: sapphire regenerative amplifier (Spectra-Physics) is employed as a laser source, with 100 fs pulse duration, 800 nm central wavelength, and 1KHz repletion rate. The laser beam shows each pulse with a certain energy of 6mJ in the entire OPTP setup. The output pulses were divided into three parts. Two of them were applied to THz wave generation and detection through ZnTe crystal. Another part of the femtosecond beam was radiating on the sample as an optical pump light. By employing a standard Fourier transformation and normalization, the frequency-dependent THz amplitude $T(\omega) = E_S(\omega)/E_R(\omega)$ was gained.

3. Results and Discussion

Figure 1a demonstrates the device fabrication process. A sandwich-structured galvanic cell is designed for optical measurements. The CVD-grown FLG film is contacted with a Li slice and covered by a few drops of electrolyte ($LiPF_6$ in ethylene carbonate/diethyl carbonate, w/w = 1:1). The sample is sealed with two thin transparent glasses and a double-sided square frame tape to prevent oxidation. Details of the device fabrication are provided in the Experiments section. Different from the conventional charging mode, galvanic reaction makes a faster Li intercalation because of the direct contact of the cathode (FLG) and anode (Li). During the Li intercalation process, the crystal structure of FLG remains unchanged because of Li-ions accommodated in the graphene interlays, as shown in Figure 1b. According to previous research, intercalation behavior often leads to a strong charge transfer between host and guest[29, 30], and the direction of interfacial charge transfer defers to interfacial level alignment regulation[30-32]. For Li intercalation on FLG, the charge transfer occurs from Li atoms to graphene layers, as illustrated in Figure 1b. Large numbers of electrons fill the π orbitals in graphene with E_f increased, as shown graphene band structure before and after Li intercalation in Figure 1c.

Figure 1. Device schematics and working principle. (a) Schematic of the fabrication of galvanic cell device. (b) The crystal structure of FLG before and after Li intercalation. LiC_{12} periodically repeats the layer along the z-axis with the stacking sequence of AAαAAα, A and α being the fictitious graphene and Li-ion layer, respectively. The direction of electron transfer from Li atoms to graphene layers is described by the deep blue arrows. Black balls represent carbon atoms and light grey balls represent Li-ions. (c) Schematic of graphene band structure before and after Li intercalation.

Raman spectroscopy is employed to characterize the structures' change of FLG with Li intercalation, as depicted in Figure 2a. Before Li intercalation, FLG shows a typical Raman spectrum (black line). The G peak is located at 1583.9 cm⁻¹, which is a normal first-order Raman scattering process and is associated with the in-plane vibrations of sp² carbon atoms[33]. The 2D peak appears at 2704.2 cm⁻¹, originating from a second-order process and involving two phonons near the Dirac point[33]. The D peak is observed at 1354.5 cm⁻¹, being a double resonance scattering process due to the presence of structural defects[34]. After Li intercalation, the Raman spectrum is shown in the red line. The G peak shows a blue shift to 1591.4 cm⁻¹ due to Li doping[12]. The 2D peak completely disappears. This is because of the strong electron transfer from Li atoms to graphene layers, leading to the inter-band optical transition Pauli-blocked[12]. Thus, there is no resonant Raman process. According to previous research, the result corresponds to the formation of LiC_{12} with a graphene layer flanked on one side by Li-ions[12, 35]. The position and intensity of the D peak remain almost unchanged, implying no obvious structural deformation during the Li intercalation process.

To investigate the carrier transport behavior of FLG film before and after Li intercalation, we transfer the sample onto pre-deposited electrical contacts with a Hall bar arrangement. The Van der Pauw technique is applied to measure the sheet resistance, which is not prone to errors due to the existence of contact resistance, as described by the $I-V$ curves in Figure 2b. Before Li intercalation (black line), the FLG presents a high resistance characteristic with a sheet resistance of 1224.5 Ω/sq. After Li intercalation ((red line), sheet resistance drops by two orders of magnitudes to 66.1 Ω/sq. According to previous research, intercalation can increase the concentration of carriers (electrons or holes)[27, 36], which can effectively enhance the material's electrical conductivity[37].
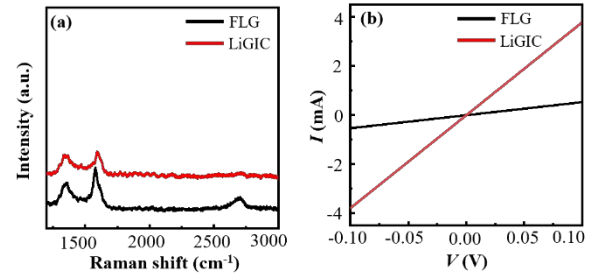
Figure 2. (a) Raman spectra of FLG before (black line) and after (red line) Li intercalation. (b) Four-probe I versus V curves for FLG before (black line) and after (red line) Li intercalation.

The demonstration of visible modulation of FLG with Li intercalation is shown in Figure 3. The devices are encapsulated with JGS1 quartz for visible optical measurements. Figures 3a and 3b show the optical images of FLG and LiGIC. Apparently, the LiGIC has a higher transparency compared with FLG. To further examine the light modulation effect of lithium intercalation, we measured the optical spectra of FLG and LiGIC in the wavelength range of 480 to 1040 nm. The transmissivity spectra are shown in Figure 3d. For FLG (black line), the transmissivity increases gradually with the wavelength, from 84.9% at 480 nm to 87.6% at 1040 nm. After Li intercalation, LiGIC (red line) has a higher transmissivity of over 90% from 480 nm to 1040 nm, with a maximum increase of 7.7% from 86.4% to 94.1% at 600 nm. The reflectivity spectra of FLG before (black line) and after (red line) Li intercalation are displayed in Figure 3e. From the wavelength of 500 to 600 nm, FLG presents almost the same reflectivity as LiGIC. From 600 to 970 nm, the reflectivity of LiGIC is higher than FLG, with an increase of 0.33% at 702 nm. From 970 to 1040 nm, the reflectivity of LiGIC is lower than FLG. The absorptivity spectra can be computed based on the transmissivity and reflectivity spectra, as illustrated in Figure 3f. The

FLG has a remarkable absorptivity change after Li intercalation over the wavelength from 480 to 1000 nm, with a maximum decrease of 7.89% from 10.99% to 3.1% at 650 nm.

The transmittance increase and absorptivity decrease indicate that graphene has a shift of E_f after Li intercalation. Li is an active alkali metal with strong electron donation capability, and Li-2s electrons tend to transfer into carbon π-bands[27]. Therefore, it results in the E_f moving into the region of the high density of states. The diagram of the doped graphene band structure and interband transition is illustrated in Figure 3c. The optical response of graphene at visible frequency depends on interband transition.[38, 39] When photon energy is lower than $2E_f$, the optical interband transitions are locked due to the Pauli Exclusion Principle. Hence, the uplift of E_f cause reduced absorption and increased transmission in the visible waveband. The transparency change in the macro-scale sample enables us to perceive the Li intercalation behavior on the micro-scale.
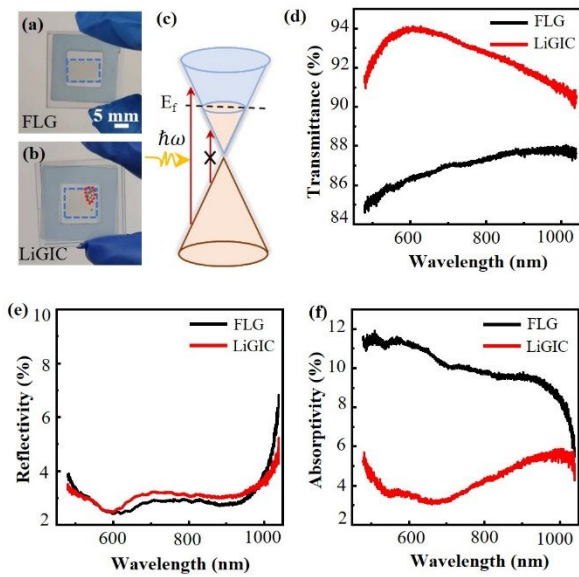

Figure 3. Demonstration of visible optical modulation of FLG with Li intercalation. (a) and (b) are visible images of FLG and LiGIC, respectively. The scale bar is 5 mm. The FLG and Li metal are marked with blue and red dotted boxes, respectively. (c) Schematic interband electronic transitions of the Li-intercalated graphene for visible absorption. (d) Optical transmittance as a function of wavelength in the visible and near-infrared range for FLG (black line) and LiGIC (red line). (e) Optical reflectivity as a function of wavelength in the visible and near-infrared range for FLG (black line) and LiGIC (red line). (f) Optical absorptivity as a function of wavelength in the visible and near-infrared range for FLG (black line) and LiGIC (red line).

In the infrared frequency band, the optical modulation of FLG by Li intercalation is displayed in Figure 4. Figure 4a illustrates a cross-section of the optical device on a hot plate for qualitative demonstration of infrared transmission. Two BaF_2 with a high infrared transmittance are applied to seal the device, as shown in Figure 4e (blue line). To increase the contrast between the sample and the background, an aluminum (Al) foil with low infrared emissivity is placed under the device. The surface temperature distribution of the devices is detected by an infrared camera with a wavelength operation range from 7.5 to 14 μm, as shown in Figure 4b. As the hot plate is fixed to 30 °C, the Al foil shows a black color

because its low infrared emissivity and low infrared transmittance result in a low apparent temperature. In the sample area marked with a blue dotted box, LiGIC shows a higher 1 °C apparent temperature than FLG. When the hot plate is fixed to 40 °C, the Al foil remains only the whole covered by the device. The LiGIC shows a higher 1.9 °C apparent temperature than FLG. For LiGIC and in the corner far away from the Li metal, we can observe a lower apparent temperature compared to other regions. This is attributed to the Li deintercalation and recovery of its optical properties.
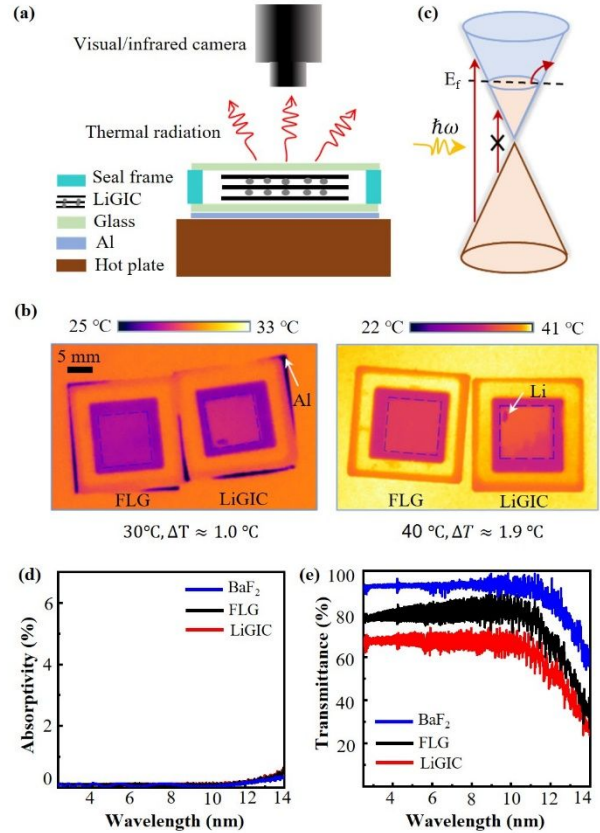

Figure 4. Demonstration of infrared optical modulation of FLG with Li intercalation. (a) Cross-sectional illustration of infrared transmission characterization by an infrared camera. The optical device is placed on a hot plate. (b) Thermal images of FLG and LiGIC, and their position with the blue dotted box marked. The hot temperature is set as 30 and 40 °C. The scale bar is 5 mm. (c) Schematic intraband and interband electronic transitions of the Li-intercalated graphene for mid-infrared absorption. (d) Optical absorptance as a function of wavelength in the infrared range for BaF_2 (blue line), FLG (black line), and LiGIC (red line). (e) Optical transmittance as a function of wavelength in the infrared range for BaF_2 (blue line), FLG (black line), and LiGIC (red line).

To better comprehend the thermal imaging temperature difference of FLG before and after Li intercalation, we additionally measured the infrared absorption and transmission spectra, as illustrated in Figures 4d and 4e. FLG shows almost the same absorption spectra as LiGIC, in which the absorptivity has a small increase with wavelength, from ~0.1% at 2.5 μm to ~0.5% at 14 μm. As for the transmission, the FLG reduces from ~80% to ~68% over the wavelength range from 2.5 to 11 μm after Li intercalation. From 11 to 14 μm, the FLG and LiGIC present a transmittance reduction with wavelength. The decreased transmittance may come from the BaF_2, as shown blue line in Figure 4e. These results are consistent with

their thermal images. Compared to FLG, LiGIC has the same optical absorption (~0%) but a lower transmittance. Therefore, LiGIC shows a higher apparent temperature than FLG with Al foil as the background. Schematic the increased E_f of the Li-intercalated graphene and the electronic transitions, is depicted in Figure 4c. The optical absorption of graphene is mainly due to the interband and intraband electron transitions[39, 40]. Graphene with low doping (E_f of 200 meV) can block infrared absorption due to interband transition. On the other hand, increased carrier concentration leads to a small enhancement of infrared absorption due to intraband transition. According to relevant studies, the mid-infrared optical absorption of graphene is very small and modulated no more than 0.25% at 14 μm by ionic liquid intercalation[37]. Therefore, when the total contributions of the two transition processes in the mid-infrared waveband are almost equivalent, FLG and lithiated graphene may illustrate the same infrared absorption.
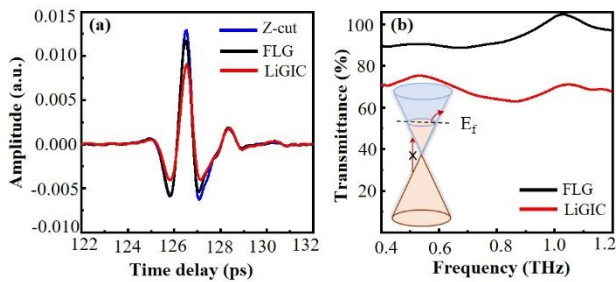

Figure 5. Demonstration of terahertz optical modulation of FLG with Li intercalation. (a) Terahertz time-domain signals of Z-cut (blue line), FLG (black line), and LiGIC (red line). (b) Spectrum of the transmitted THz signal of FLG (black line) and LiGIC (red line) is obtained through Fourier transform time-domain signals and normalization with the reference signal. The inset is schematic intraband electronic transitions of the Li-intercalated graphene for THz absorption.

The THz response is measured by conventional THz time-domain spectroscopy. Two Z-cut quartz without FLG is regarded as a reference. Figure 5a shows the time-domain signal of Z-cut (blue line), FLG (black line), and LiGIC (red line). It can be observed that Li intercalation makes a remarkable change in the peak amplitude of the THz pulse. With the Fourier transform of time-domain signals and normalization with the reference signal, we obtained transmitted THz amplitude spectra, as shown in Figure 5b. For FLG (black line), the average of the transmitted signal is ~90% from 0.4 to 1.2 THz. After Li intercalation (red line), the amplitude of the transmitted signal shows about 20% modulation over broad spectra from 0.4 to 1.2 THz and decreases from 97.2% to 68.2% at the wavelength of 1.2 THz. The set of Figure 5b shows electronic transitions of the Li-intercalated graphene. For the long wavelengths of terahertz frequencies, the interband transitions are Pauli-blocked even an unintentional doping. Therefore, the long-wavelength optical absorption is mainly due to the low-energy intraband transition[41]. In the THz regime, graphene is regarded as tunable Drude metal and its optical conductivity depends on frequency expressed as equation (1) [42,43]

$$\sigma(\omega)_{intra} = \frac{\sigma_{DC}}{1 + j\omega\tau} \qquad (1)$$

where σ_{DC}, τ, and ω is the conductivity of graphene, scattering time of graphene, and frequency, respectively. Therefore, the direct current conductance is beneficial to the increase of THz optical absorption. As shown in Figure 2b, Li intercalation leads to striking resistance reduction of FLG. Thus, it will make an enhancement of THz optical absorption, which imply the decrease in transmission (Figure 5b).

4. Conclusion

In conclusion, we have developed the Li-intercalated FLG with a galvanic cell structure, realizing the broadband optical modulation of FLG, with visible transparency increase and higher than 90% from the wavelength of 480 to 1040 nm, with infrared transmittance decrease from ~80% to ~68% in the wavelength range from 2.5 to 11 μm, and with ~20% reduction in the wavelength range from 0.4 THz to 1.2 THz. This is attributed to the strong electron doping resulting in the uplift E_f of graphene, which makes significant changes in the intraband and interband optical transitions. The visible, mid-infrared, and THz optical responses are attributed to interband transitions, intraband and interband transitions, and intraband transitions, respectively. Our research may provide a new strategy for the design of optical modulation devices in a broad spectra region.

References

1. Y. Zhang, J. Shen, J. Li, et al., "High-speed electro-optic modulation in topological interface states of a one-dimensional lattice," Light Sci. Appl. 12, 206 (2023).
2. Z. Zhou, R. Song, J. Xu, X. Ni, Z. Dang, et al., "Gate-tuning hybrid polaritons in twisted α-MoO₃/graphene heterostructures," Nano Lett 23, 11252-11259 (2023).
3. W. Zhao, B. Shen, et al., "Gate-tunable heavy fermions in a moiré Kondo lattice," Nature 616, 61-65 (2023).
4. B. Zheng and G. X. Gu, "Machine learning-based detection of graphene defects with atomic precision," Nano-Micro Lett. 12, 181 (2020).
5. P. Huang, et al., "Unveiling the complex structure-property correlation of defects in 2D materials based on high throughput datasets," NPJ 2D Mater. 7, 6 (2023).
6. S. Yang, Y. Chen, C. Jiang, "Strain engineering of two-dimensional materials: Methods, properties, and applications," InfoMat 3, 397-420 (2021).
7. M. Kapfer, et al., "Programming twist angle and strain profiles in 2D materials," Science 381, 677-681 (2023).
8. K. Bi, et al., "High-performance lateral MoS₂-MoO₃ heterojunction phototransistor enabled by in-situ chemical-oxidation," Sci. China Mater. 63, 1076-1084 (2020).
9. X. Zhu, Y. Cheng, F. Chen, H. Luo, and W. Ling, "Efficiency adjustable terahertz circular polarization anomalous refraction and planar focusing based on a bi-layered complementary Z-shaped graphene metasurface," J. Opt. Soc. Am. B 39, 705-712 (2022).
10. D. Yang, Y. Cheng, F. Chen, H. Luo, L. Wu, "Efficiency

tunable broadband terahertz graphene metasurface for circular polarization anomalous reflection and plane focusing effect," Diam. Relat. Mater. 131, 109605 (2023).

11. J. Zhang, A. Yang, X. Wu, et al., "Reversible and selective ion intercalation through the top surface of few-layer MoS_2," Nat. Commun. 9, 5289 (2018).

12. W. Bao, et al., "Approaching the limits of transparency and conductivity in graphitic materials through lithium intercalation," Nat. Commun. 5, 4224 (2014).

13. M. Wang and K. J. Koski, "Reversible chemochromic MoO_3 nanoribbons through zerovalent metal intercalation," ACS Nano 9, 3226-3233 (2015).

14. Y. Bao, Y. Han, L. Yang, N. Li, J. Luo, et al., "Bioinspired controllable electro-chemomechanical coloration films," Adv. Funct. 29, 1806383 (2019).

15. G. Zeng, R. Zhang, Y. Sui, et al., "Inversion symmetry breaking in lithium intercalated graphitic materials," ACS Appl. Mater. Interfaces 12, 28561-28567 (2020).

16. G. Zeng, Z. Fang, C. Qin, L. Xiao, S. Jia, "Intercalating-induced second-harmonic generation in centrosymmetric multilayer graphene," Appl. Phys. Lett. 122(2023).

17. C. Zhang, G. Zeng , R. Zhang, et al., "Tunable nonlinear optical responses of few-layer graphene through lithium intercalation," Nanophotonics 10, 2661-2669 (2021).

18. O. Salihoglu, H. Uzlu, et al., "Graphene-based adaptive thermal camouflage," Nano Lett 18, 4541-4548 (2018).

19. J. Wan, Y. Xu, B. Ozdemir, et al., "Tunable broadband nanocarbon transparent conductor by electrochemical intercalation," ACS Nano 11, 788-796 (2017).

20. K. F. Mak, L. Ju, F. Wang, T. F. Heinz, et al., "Optical spectroscopy of graphene: From the far infrared to the ultraviolet," Solid State Commun. 152, 1341-1349 (2012).

21. R. R. Nair, et al., "Fine structure constant defines visual transparency of graphene," Science 320, 1308-1308 (2008).

22. X. Y. Song, et al., "Microstructural characterization of lithiated graphite," J. Electrochem. Soc. 143, L120 (1996).

23. S. K. Tiwari, S. Sahoo, N. Wang, and A. Huczko, "Graphene research and their outputs: Status and prospect," J SCI-ADV MATER DEV. 5, 10-29 (2020).

24. N. Liu, Q. Tang, B. Huang and Y. Wang, "Graphene synthesis: method, exfoliation mechanism and large-Scale Production," Crystals, (2022).

25. S. Han, "Structure and dynamics in the lithium solvation shell of nonaqueous electrolytes," Sci. Rep. 9, 5555 (2019).

26. K. Karuppasamy, C. V. Vani, R. Antony, S. Balakumar, et al., "Effect of succinonitrile and nano-hydroxyapatite on ionic conductivity and interfacial stability of polyether-based plasticized nanocomposite polymer electrolytes (PNCSPE)," Polym. Bull. 70, 2531-2545 (2013).

27. K. Kanetani, K. Sugawara, et al., "Ca intercalated bilayer graphene as a thinnest limit of superconducting C_6Ca,"

PNAS. 109, 19610-19613 (2012).

28. I. P. Batra and L. Samuelson, "A theoretical study of the electronic properties of intercalated graphite," Synth. Met. 1, 233-247 (1980).

29. Y. Sun, C. Zhang, F. Zhang, D. Zhou, et al., "$FeCl_3$ intercalated microcrystalline graphite enables high volumetric capacity and good cycle stability for lithium-ion batteries," Energy Technol. 7, 1801091 (2019).

30. F. Xiong, et al., "Li intercalation in MoS2: in situ observation of its dynamics and tuning optical and electrical properties," Nano Lett 15, 6777-6784 (2015).

31. J. Zheng, et al., "Diffusion of Li^+ ion on graphene: A DFT study," Appl. Surf. Sci. 258, 1651-1655 (2011).

32. P. Beyer, E. Meister, T. Florian, et al., "Fermi level pinned molecular donor/acceptor junctions: reduction of induced carrier density by interfacial charge transfer complexes," J. Mater. Chem. 8, 15199-15207 (2020).

33. L. M. Malard, M. A. Pimenta, et al., "Raman spectroscopy in graphene," Phys. Rep. 473, 51-87 (2009).

34. S. Gómez, N. M. Rendtorff, E. F. Aglietti, et al., "Surface modification of multiwall carbon nanotubes by sulfonitric treatment," Phys. Rep. 379, 264-269 (2016).

35. T. Liang, et al., "Modulating visible-near-infrared reflectivity in ultrathin graphite by reversible Li-ion intercalation," Opt. Mater. 121, 111517 (2021).

36. S. Seiler, C. E. Halbig, F. Grote, et al., "Effect of friction on oxidative graphite intercalation and high-quality graphene formation," Nat. Commun. 9, 836 (2018).

37. G. Zeng, et al., "Graphene-based tunable coloration film through intercalation," ACS Photonics 8, 3599-3606 (2021).

38. I. Alonso Calafell, et al., "Giant enhancement of third-harmonic generation in graphene–metal heterostructures," Nat. Nanotechnol. 16, 318-324 (2021).

39. L. M. Malard, et al., "Observation of intra- and inter-band transitions in the transient optical response of graphene," New J. Phys. 15, 015009 (2013).

40. J. Wang, et al., "Optoelectronic and photoelectric properties and applications of graphene-based nanostructures," Mater. Today Phys.13, 100196 (2020).

41. K. Nakagawa, S. A. Sato, H. Tahara, et al., "Size-controlled quantum dots reveal the impact of intraband transitions on high-order harmonic generation in solids," Nat. Phys. 18, 874-878 (2022).

42. N. Kakenov, O. Balci, E. O. Polat, H. Altan, and C. Kocabas, "Broadband terahertz modulators using self-gated graphene capacitors," J. Opt. Soc. Am. B 32, 1861-1866 (2015).

43. C.-J. Yang, J. Li, M. Fiebig and S. Pal, "Terahertz control of many-body dynamics in quantum materials," Nat. Rev. Mater. 8, 518-532 (2023).